International Journal of Heat and Fluid Flow 29 (2008) 1258–1267

Contents lists available at ScienceDirect

International Journal of Heat and Fluid Flow

journal homepage: www.elsevier.com/locate/ijhff

Local heat transfer enhancement around a matrix of wall-mounted cubes using passive flow control: Large-eddy simulations

H. Hemida *, F. Spehr, S. Krajnović

Division of Fluid dynamics, Department of Applied Mechanics, Chalmers University of Technology, SE-412 96 Gothenburg, Sweden

ARTICLE INFO

Article history:
Received 14 June 2007
Received in revised form 13 December 2007
Accepted 1 April 2008
Available online 4 June 2008

Keywords:
CFD
Vortex generators
LES
Heat transfer
Bluff body flow
Passive flow control

ABSTRACT

The purpose of the research reported in this paper was to investigate the influence of attaching vortex generators (VGs) to a surface of a heated cube on flow structures and heat transfer using large-eddy simulation (LES). The cube was located in the middle of a matrix of similar cubes. Two kinds of vortex generators were investigated. The first kind was a simple rib extending in the span-wise direction (VG1) while the second consisted of several of small cubes (VG2). The flow and heat transfer around a cube with vortex generators were compared with the flow and heat transfer around a smooth cube. The LES results showed that the flow in the boundary layer around the cubes with VGs is more turbulent and unsteady than the flow around the smooth cube. More complex structures are generated close to the surface of the cube with VGs, resulting in a considerable increase in the heat transfer coefficient. Local overheating was found behind the rib-shape VG while even distribution of temperature was observed over the surfaces of the cube in the VG2 case. There was a 14% and 17% global increase in the heat transfer coefficient in the VG1 and VG2 cases, respectively.

1. Introduction

When electronic components are attached to a printed circuit, they act, under concentrated heat dissipation conditions, as a strong source of heat which might cause local overheating. It is generally believed that local overheating of integrated circuits (IC) is the major cause of the technical failure of electronic equipment (Meinders and Hanjalić, 2002). Hence, finding a way to efficiently remove heat from these components is crucial for ensuring reliable long-term operations. The production and development of new generations of power electronic components are controlled by an efficient design that removes the heat generated by these components. In general, the heat removal from an integrated circuit is very dependent on the flow structure around it (Ničeno et al., 2002).

The electronic component is a bluff body and the flow around it is dominant with separation and recirculation regions. The flow around an integrated electronic circuit can be approximated to be similar to that around a cube mounted on a surface. Previous investigations of the flow around a single surface-mounted cube found that different kinds of flow instabilities give rise to different flow structures around the cube. At very low Reynolds numbers, the flow is laminar everywhere around the cube. The flow might separate from the sides of the cube to form separation bubbles that might also be laminar. The flow inside these bubbles circulates, and it might be trapped in place if the bubbles are steady. At a certain critical Reynolds number, the shear layer's instability between the separation bubbles and the exterior fluid (the so-called Kelvin–Helmholtz flow instability) precedes the transition to turbulence and turbulent flow onsets downstream of the separation region. This flow instability is responsible for shedding vortex tubes in a regular fashion to the wake flow behind the cube, distortion of large-scale vortices, production of small-scales and eventually transition from laminar to turbulent flow in the wake. Beyond this critical Reynolds number, the flow is fully turbulent behind the cube. There is also a flow instability in the wake flow behind the cube, which is associated with the shedding of large-scale vortices from the recirculation region to the far wake flow. This flow instability is controlled by the flow Reynolds number and hence the high frequency mode in the shear layers between the recirculation region and the surrounding fluid. The dominant shear layers around the cube make the flow structures very complicated.

Different numerical methods have been used in the past to study the flow around a single cube mounted on a surface. Krajnović and Davidson(2000, 2002) used large-eddy simulation to investigate the flow structures around a surface-mounted cube in fully developed channel flow. In their simulations, the Reynolds number was 4×10^4 based on the incoming mean bulk velocity and the height of the cube. They found that the flow separates from the surface of the cube on the lateral and on the top-side faces. They visualized a horse shoe vortex attached to the mounting surface.

* Corresponding author.
E-mail address: hassan.hemida@epsilon.nu (H. Hemida).

0142-727X/$ - see front matter © 2008 Elsevier Inc. All rights reserved.
doi:10.1016/j.ijheatfluidflow.2008.04.005

Cone-like vortices are formed on the top-side face and an arch-like vortex was visualized in the wake flow. These complex flow structures were obtained using different flow simulations. The results were in good agreement with the experimental results of Martinuzzi and Tropea (1993). Yakhot et al. (2006) studied the same cube using direct numerical simulation (DNS) and they observed similar flow structures.

The turbulent flow around multiple cubes is even more complicated. The wake structures from one cube interact with the structures of the next cubes. The flow is characterized by the distance between the cubes and their arrangement in the matrix. The complex topology of the cubes induces the flow to separate and recirculate locally between the mounting surface and the cubes. The shedding of the large-scale structures in the wake flow depends mainly on the Reynolds number of the flow and on the separation distance between the cubes. The flow structures, however, are highly unsteady and three-dimensional.

At present, there are remarkably few studies on the convective heat transfer around a three-dimensional object (Nakamura et al., 2003). Meinders and Hanjalić (1999) experimentally investigated the influence of the relative position of the obstacle on the convective heat transfer from a configuration of two wall-mounted cubes located in a fully developed turbulent channel. They found that the crucial parameter that influences the flow pattern and, consequently, the heat transfer is the longitudinal spacing between the cubes. Meinders and Hanjalić (2002) also carried out experiments in a matrix of equidistant cubes mounted on one of the walls of a plane channel. Their investigation provided reference data on flow and heat transfer relevant to electronics circuitry. They studied an internally heated cube that was placed in the middle of a matrix of identical but non-heated cubes; all were mounted on a constant temperature channel wall (see Meinders and Hanjalić, 2002; Niĉeno et al., 2002). The surrounding cubes on the matrix ensured a fully developed flow with periodic boundary conditions. Because of the well-known boundary conditions and their computational simplicity, their case and data were considered as a basis for many computational fluid dynamic simulations made to gain insight into the physics of the flow structures and heat transfer. Verstappen et al. (2000) made a numerical simulation of the turbulent flow and heat transfer in a channel with surface-mounted cubical obstacles without using any turbulent models. They used a $64 \times 64 \times 32$ grid to make a DNS in a domain consisting of one cube mounted at the middle of the matrix. They used a fourth-order discretization scheme. The DNS flow profiles agreed well with the available experimental data. The time-averaged surface temperature agreed well with the experimental data except for at the edges of the cube, where differences up to 10 % exist. Cheng et al. (2003) and Zhong and Tucker (2004) used the experimental data of Meinders and Hanjalić (2002) to compare different simulation techniques (large-eddy simulation (LES), standard k–ϵ Reynolds-averaged Navier–Stokes (RANS) and k–l based hybrid LES/RANS).

Despite the many attempts that have been made to understand the physics of the flow around single or multiple cubes, there have been very few attempts to find a way to enhance heat transfer around the cubes.

In this paper, we investigate the enhancement of heat transfer by altering the turbulent boundary layer. This is done by generating small vortices on the surface of the cube using vortex generators (VGs). Two types of VGs were investigated in this paper. The first type is a simple rib while the second consists of 15 small cubes attached to the top and lateral sides of the large cube. The two vortex generators are mounted at the same position on the top and the lateral faces of each cube in the matrix. The Reynolds number of the flow is 13,000, based on the incoming bulk velocity and the height of the channel. The purpose of the present work is to employ LES to investigate the influence of the vortex generators on the flow structures and the local heat transfer coefficient.

2. Physical model

The physical model is a single heated cube placed in the middle of an equidistant matrix of surface-mounted cubes as shown in Fig. 1. The matrix of cubes is placed on one of the vertical walls of a two-dimensional channel. The matrix consists of a total of 25×10 cubes in the stream-wise and span-wise directions, respectively. The length of the side of cubes, H, is 15 mm. The height of the channel is 51 mm ($3.4H$). The distance between the centerlines of any two successive cubes in both the stream-wise and span-wise directions is 60 mm ($4H$). The vortex generators used here are described in Section 5 of this paper.

3. Governing equations

Since the flow is unsteady, an unsteady numerical method for the prediction of the flow and heat transfer is needed. Direct numerical simulation (DNS) is computationally demanding due to the very large number of nodes needed to resolve all the flow scales. The flow around a cube is a typical bluff body flow that is dominated by large separation and recirculation regions. Previous investigations of the flow around bluff bodies showed that Reynolds-averaged Navier–Stokes (RANS) methods give poor results compared to large-eddy simulations (LES). In this paper, LES was employed to solve for both the velocity and temperature fields. In LES, the large-eddies are computed directly and the influences of the small-scale eddies on the large-scale eddies are modeled. The incompressible continuity, momentum and energy equations are filtered using an implicit spatial filter. The resulting filtered equations are:

$$\frac{\partial \bar{u}_i}{\partial x_i} = 0, \tag{1}$$

$$\frac{\partial \bar{u}_i}{\partial t} + \frac{\partial}{\partial x_j}(\bar{u}_i \bar{u}_j) = -\frac{1}{\rho}\frac{\partial \bar{p}}{\partial x_i} + \nu \frac{\partial^2 \bar{u}_i}{\partial x_j x_j} - \frac{\partial \tau_{ij}}{\partial x_j} \tag{2}$$

and

$$\frac{\partial \overline{T}}{\partial t} + \frac{\partial}{\partial x_j}(\bar{u}_j \overline{T}) = \frac{\nu}{Pr}\frac{\partial^2 \overline{T}}{\partial x_j x_j} - \frac{\partial h_j}{\partial x_j}. \tag{3}$$

Here, $\bar{u}_i$, $\overline{P}$ and $\overline{T}$ are the resolved filtered velocity, pressure and temperature, respectively. Owing to the non-linear terms in the momentum and heat equations, the filtered-out small-scale eddies feed back their effects on the large-scale motion through sub-grid scale stresses and heat fluxes. These influences appear as extra terms in the filtered equations, i.e. τ_{ij} and h_j. The sub-grid scale (SGS) stresses, $\tau_{ij} = \overline{u_i u_j} - \bar{u}_i \bar{u}_j$, represent the influence of the unresolved scales, smaller than the filter size, on the resolved ones. The sub-grid heat fluxes, $h_j = \overline{u_j T} - \bar{u}_j \overline{T}$, represent the influence of the unresolved heat fluxes on the resolved ones.

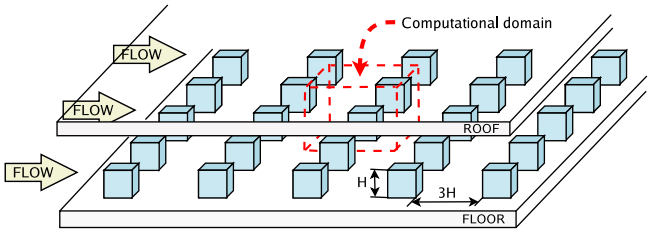

Fig. 1. Matrix of cubes mounted in a channel.

These sub-grid stresses and heat fluxes are unknowns and must be modeled. The standard Smagorinsky model was used in the present work to model the SGS stresses and the heat fluxes. This model was used for its simplicity and to reduce computational cost. In this model, the sub-grid scale stresses and heat fluxes are modeled as

$$\tau_{ij} - \frac{1}{3}\delta_{ij}\tau_{kk} = -2\nu_{sgs}\overline{S}_{ij} \tag{4}$$

and

$$h_j = -2\alpha_t \frac{\partial \overline{T}}{\partial x_j}, \tag{5}$$

where ν_{sgs} is the sub-grid scale viscosity, α_t is the sub-grid scale eddy diffusivity and $\overline{S}_{ij}$ is the resolved rate of the strain tensor defined as

$$\overline{S}_{ij} = \frac{1}{2}\left[\frac{\partial \bar{u}_i}{\partial x_j} + \frac{\partial \bar{u}_j}{\partial x_i}\right]. \tag{6}$$

The sub-grid scale viscosity, ν_{sgs}, is defined as:

$$\nu_{sgs} = (C_s \Delta)^2 |\overline{S}|, \tag{7}$$

where the magnitude of the local strain rate tensor is defined by $|\overline{S}| = \sqrt{2\overline{S}_{ij}\overline{S}_{ij}}$, Δ is the filter width taken as the cubic root of the volume of the finite volume cell and C_s is the model constant. The value of the model constant, C_s, in the present work was 0.1. Similar to the sub-grid scale viscosity, the sub-grid scale eddy diffusivity, α_t, is defined as

$$\alpha_t = \frac{1}{Pr_t}(C_s \Delta)^2 |\overline{S}|, \tag{8}$$

where Pr_t is the sub-grid scale Prandtl number. The value of Pr_t was taken as 0.6 in this paper. The Smagorinsky model is widely used in simulations of bluff body flow (see Hemida et al., 2005; Krajnović and Davidson, 2005; Barhaghi et al., 2006). It is also used to model the unresolved fluxes in the simulations of heat transfer problems (see Barhaghi et al., 2006).

4. Computational domain and boundary conditions

The size of the computational domain is $4H \times 3.4H \times 4H$. Similar to the experimental set-up of Meinders and Hanjalić (2002), the test cube is chosen to be in the middle of the matrix of cubes, where the flow is fully developed in both the stream-wise and the span-wise directions. Due to the periodicity of the flow around the cubes, periodic boundary conditions are applied in the stream-wise and the span-wise directions for the velocity field. No-slip boundary conditions are employed at solid walls.

The x and y axes are in the stream-wise and wall-normal directions, respectively, while the z-direction denotes the span-wise direction. The coordinate system originates from the channel wall at the center of the windward face of the cube. The bulk velocity of the incoming flow is 3.86 m/s, yielding a Reynolds number of 13,000, based on the incoming bulk velocity and the height of the channel. The density of the air is 1.16 kg/m^3 and its dynamic viscosity is 1.5×10^{-5} m^2/s. A constant mass flow rate of 0.0137 kg/s passes through the computational domain. The value of the Prandtl number of the air is 0.71.

The rate of heat dissipated from an individual cube to the air is constant and equal to 2 W. This makes the temperature rise between any two successive cubes to be constant. A uniform heat flux of 1777.8W/m^2 is used as a Neumann boundary condition for the temperature at the surface of the cube. Periodic boundary conditions for the temperature and the temperature rise are applied in the span-wise and stream-wise directions, respectively. The bulk temperature for the incoming flow, T_{bi}, is 294 K. The floor and the roof of the channel are insulated.

The thermal boundary conditions used in our LES are not the same as those used in the experimental work of Meinders and Hanjalić (2002). We simplified the thermal boundary conditions to reduce the computational cost. In their experiment, they used a heated copper core maintained at a constant temperature. The copper is coated with a layer of low-conductivity epoxy. The ratio of thermal diffusivities for air and the cube's epoxy layer is about 180. This ratio is equivalent to the characteristic time-scale ratio of the temperature evolution in the fluid and the solid. Using conjugate convection–conduction solutions with this ratio, a long time is required before reaching a statistically stationary state for the temperature field, which is required for the comparison between the different vortex generator cases. While the aim of the paper is to present the relative effect of the vortex generators, we decided to reduce the computational cost by choosing simpler thermal boundary conditions.

The FLUENT 6.3 commercial finite volume solver was employed to solve the filtered equations. The convective and viscous diffusion plus the sub-grid scale fluxes are approximated by a second-order accurate central differencing scheme. The time integration was done using the Crank–Nicholson second-order scheme.

5. Vortex generators

Vortex generators (VGs) are small devices primarily used to suppress the formation of the separation regions and to alter the aerodynamic coefficients by changing the flow structures around the bodies. As an example, VGs are used on the wing of airplanes to prevent separations and hence increase the lift coefficient. They are used inside gas turbines to reduce the pressure drop caused by flow separation (Wallin and Eriksson, 2006). The influence of the flow separation is always negative for the aerodynamic coefficient and pressure drop. In the case of heat transfer, flow separation might enhance or discard the heat transfer. The points where the flow starts to separate and where the flow reattaches to the body are always associated with a local increase of the heat transfer coefficient owing to the high turbulent intensity in the shear layers close to these points. On the other hand, the flow trapped in the separation regions and recirculation regions undergoes local heating, reducing the heat transfer coefficient.

To enhance the heat transfer from the surface of the cubes, it is highly desirable that the boundary layers on the surface of the cubes are turbulent. The turbulent boundary layer implies high local mixing because of the small-scale vortices and hence high convective heat transfer coefficients.

One way to attain a turbulent boundary layer on the surface of the cubes is to use vortex generators (VGs). These VGs are very small devices attached to the surface of the cube in the places where boundary layer separation is expected. Another advantage of the VGs is the formation of large-scale vortices behind them. These new large structures on the surface of the cube help to carry the heat from the boundary layer to the outer flow. The shape of the VGs determines to a great extent the shape of these vortices. These vortices are highly unsteady and are shed from the recirculation region behind the VGs at a regular frequency (the shedding frequency of the wake behind the VGs). The size of these vortices is in the order of magnitude of the size of the VGs, which is in the order of magnitude of the height of the boundary layer thickness without the VGs. This means that the new boundary layer on the surface of the cube with VGs is dominated by vortices that are more turbulent, unsteady and larger in scale than those in the boundary layer without VGs.

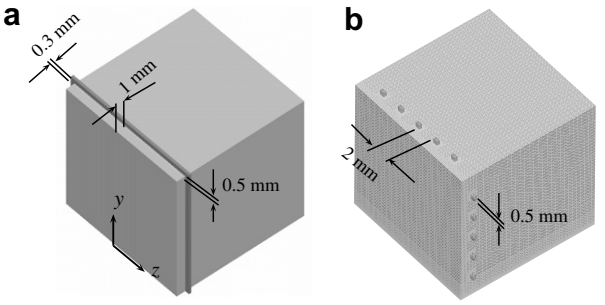

Fig. 2. The shape of the vortex generators: (a) the simple rib VG, VG1, and (b) the small cube VG, VG2.

Two kinds of VGs are used in the present work. The shape of these VGs is shown in Fig. 2. The first kind, VG1, is a simple rib attached to the top and lateral faces of the cube at a distance of 1 mm from the windward edge. The thickness of the VG is 0.3 mm and its height is 0.5 mm. The second kind of vortex generator, VG2, consists of five small cubes attached to the top-side face and five small cubes attached to each side of the lateral faces. Similar to VG1, these small cubes are at a distance of 1 mm from the front edges of the cube. The thickness and the height are identical to those of VG1. The width of each cube is 0.5 mm and the gap between any two successive cubes is 2 mm.

6. Computational grid

Hexa-hedral computational grids consisting of *O* and *C*-grid topologies are used in all of our simulations. The shapes of these grids around the cube with VG2 are shown in Fig. 3. Similar grid topologies (not shown here) are used around the smooth cube and the cube with VG1. The ICEM-CFD commercial package is used to generate the hexa-hederal cells. The total number of nodes is 400,000 for the simulation over the cube without VG. Fifteen nodes covering the height of the VG are used to resolve the flow in the wake of the VG. As a result, the computational grid for the case with VG increased to 900,000 nodes. In the case of VG2, an *O*-grid topology is used around the small cubes, as shown in Fig. 3.c and d. Using this topology reduces the number of nodes to 450,000 in the case of VG2.

The centers of all the near-wall cells have a normal distance of 0.006 mm (0.0004*H*) from the wall. This distance assures that the wall-normal distance, y^+, is less than one for the first row of cells next to the wall. The time-averaged spatial resolution in the stream-wise direction, $x^+ = \Delta l u^*/\nu$, and span-wise direction, $z^+ = \Delta\varpi su^*/\nu$ (n is the normal distance from the center of the cell to the surface of the cube, Δs is the stream-wise length of a cell, Δl is the span-wise length of a cell and u^* is the friction velocity), are shown in Table 1. Since a second-order accurate central difference scheme was used in the discretization of both the convective and diffusive terms, which is sensitive to grid stretching, the maximum stretching ratio of the grid is kept to 1.1 for any two successive nodes. To assure that the results are independent of the mesh, a second finer mesh consisting of 760,000 nodes, is generated around the cube with VG2. For isotropic and homogeneous turbulence, the Kolmogorov's length scale, $\eta_k = (\nu^3/\varepsilon)^{1/4}$ (ε is the mean dissipation rate of the turbulence energy), is the smallest scale to be spatially resolved. If we assume the large velocity scale, U, to be the bulk velocity and the integral scale, ℓ, to be the length of the edge of

Table 1
Time-averaged spatial resolution for the first cells-layer around the cube

Mesh	$y^+ = \frac{nu^*}{\nu}$	$z^+ = \frac{\Delta s u^*}{\nu}$	$x^+ = \frac{\Delta l u^*}{\nu}$
Maximum	0.8	80	80
Mean	0.3	25	25

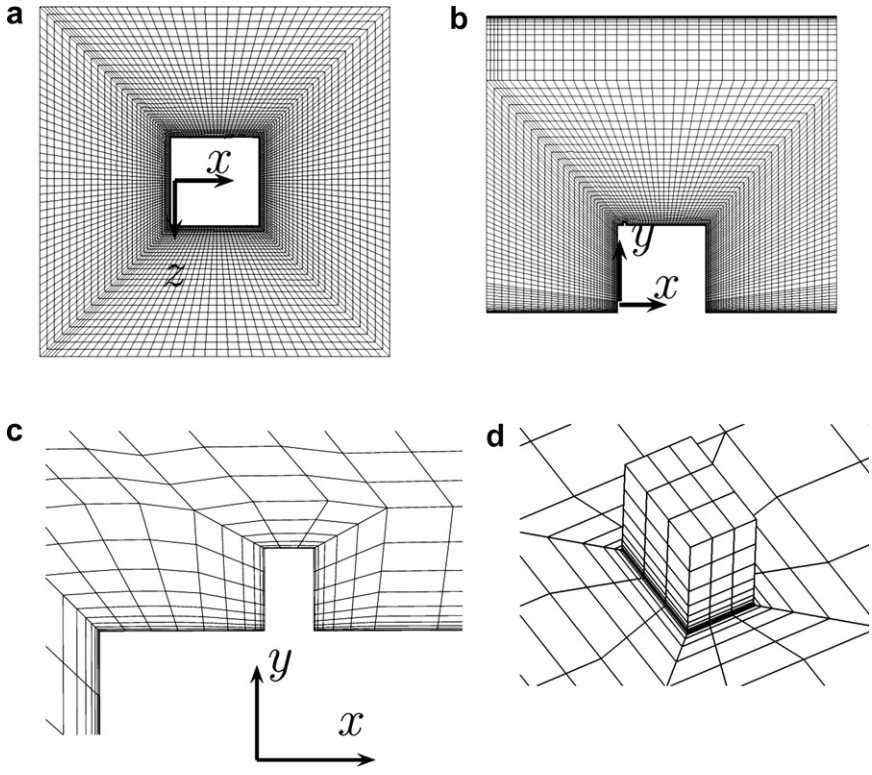

Fig. 3. The grids around the cubes with VG2: (a) and (b) the shape of the mesh in the computational domain, (c) and (d) the *O* and *C*-grids around a small cube VG.

the cube, the mean dissipation rate, ε, can be estimated from the integral velocity and length scales to be $\varepsilon = U^3/\ell \approx 3800\ \mathrm{m}^2/\mathrm{s}^3$. This gives an estimated Kolmogorov's length scale of 3×10^{-5} m. Close to the edges of the large cube and around the small cubes vortex generators, the mesh resolution is fine enough to be close to the Kolmogorov's scale. At the center of the faces of the cube, the size of the cell, $\Delta = (\Delta_x \Delta_y \Delta_z)^{1/3}$ (Δ_x, Δ_y and Δ_z are the cell length in the x, y, and z directions, respectively), is about 0.2 mm. The size of the cells in this region is very large in comparison to the Kolmogorov's scale.

7. Results

This section explores the influence of the VGs on the time-averaged flow, the instantaneous flow and the heat transfer coefficient. The simulations are made using a constant time step of 0.00015 s, yielding a maximum CFL number of less than 1.0 during the entire simulations. The entire flow field is initialized with a uniform stream-wise velocity equal to the bulk velocity of the inlet flow. The other two components of the velocity are set to zero value. The momentum equation is solved first while the energy equation is turned off. After the solution is converged and a fully developed flow is obtained, the energy equation is activated while the velocity field is frozen. When a converged solution is obtained for the temperature field, the solver for the velocity field is activated again. After fully developed turbulent flow and heat transfer are obtained, the averaged process starts. The time-averaged data are obtained using 20,000 time steps.

Two computations with different numbers of nodes (fine mesh with 760,000 nodes and coarse mesh with 450,000) are performed around the cube with VG2 to show the dependency of the results on the grid. Fig. 4 shows nine, time-averaged stream-wise and span-wise, velocity profiles obtained from the coarse and fine meshes. The profiles are on the vertical xy-plane at $z = 0$. Despite some discrepancies in the upstream boundary layer, the results obtained in the coarse mesh are in good agreement with the results of the fine mesh, meaning that any further increase in the number of nodes would not influence the results. Hence, the resolution of the coarse mesh is fine enough to be used for the comparison between the cubes with and without vortex generators.

Meinders and Hanjalić (2002) found that the shedding frequency corresponds to a Strouhal number of $St = 0.109$ based on the height of the cube and the incoming bulk velocity. In our case, it leads to a shedding frequency of about 5 cycles/s. This means that the time-averaged data are gathered over 15 shedding cycles.

Fig. 5 compares the experimental stream-wise velocity distribution from (Meinders and Hanjalić, 2002) with our LES values, obtained over the cube without VG, on the vertical xy-plane at $z/H = 0$ at five different locations: $x/H = -0.3$, $x/H = 0.5$, $x/H = 1.5$, $x/H = 1.7$ and $x/H = 2$. The figure shows good agreement between the LES data and the experimental data, verifying that the mesh resolution is fine enough to resolve the flow and hence the heat transfer.

Fig. 6a and b displays the time-averaged flow structures around the smooth cube by means of streamlines projected to the xy-plane and xz-plane at $z/H = 0$ and $y/H = 0.5$, respectively. The flow impinges on the stream-wise face of the cube, causing a stagnation region with high pressure. The stagnation line can be seen in Fig. 6a at $y/H \simeq 0.8$. Due to the high pressure in the stream-wise face, the flow moves up, down and towards the lateral faces. Because of the impingement on the mounting ground, the part of the flow that moves downward is forced to change direction to circulate around the cube, forming the horse shoe-like vortex. The part of the flow that moves towards the top and lateral faces separates from the surfaces of the cube before it reattaches again to the surface. The separation bubbles are shown in Fig. 6.

Fig. 6a shows a clear circulation bubble in the wake flow with a focus that is above $y/H = 0.5$. The axis of this bubble is parallel to the span-wise direction (z-axis). Fig. 6b shows two recirculation regions in the wake flow of the cube. The flow coming from the sides of the cube separates from the surface and circulates to form these recirculation bubbles. The axes of these recirculation bubbles are parallel to the normal direction of the mounting surface (y-axis). These two vortices are connected to each other through the upper-side vortex to form an arch-shaped vortex behind the cube.

The time-averaged flows around the cubes with VGs are explored by flow patterns similar to those in Fig. 6 (not shown here). These flow patterns show that the time-averaged flow structures around the cubes with VGs are similar to those around the smooth cube. A difference can be found by zooming in these separation

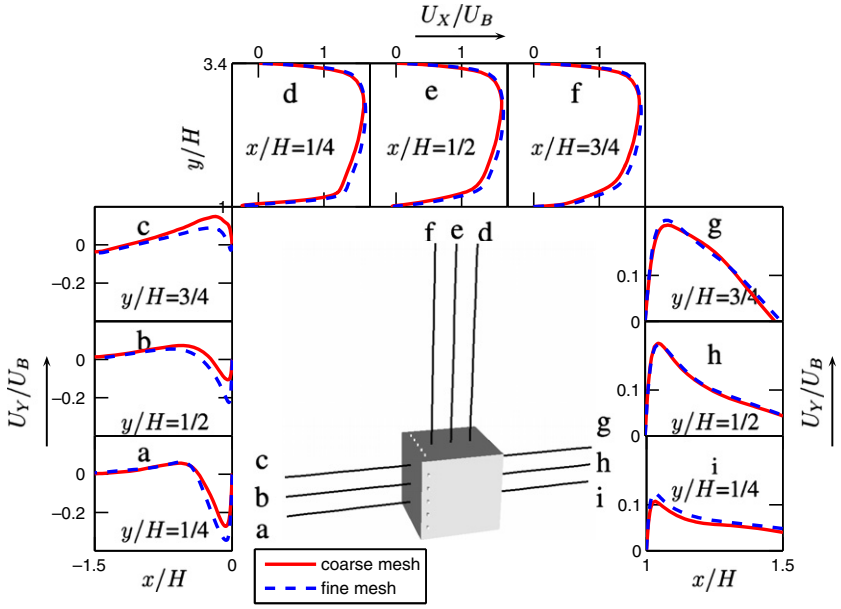

Fig. 4. LES time-averaged stream-wise and span-wise velocity profiles at different positions around the cube with VG2 in the $z = 0$ plane.

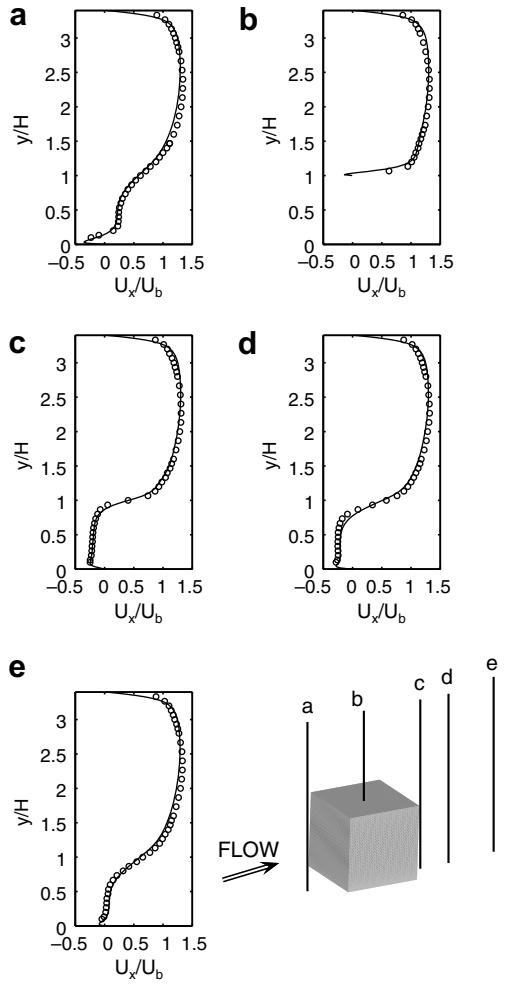

Fig. 5. Time-averaged stream-wise velocity profiles around a smooth cube on the vertical xy-plane: $z = 0$ at (a) $x/H = -0.3$, (b) $x/H = 0.5$, (c) $x/H = 1.3$, (d) $x/H = 1.5$, (e) $x/H = 2$. Symbols: experimental results from Meinders and Hanjalić (2002); solid line: LES.

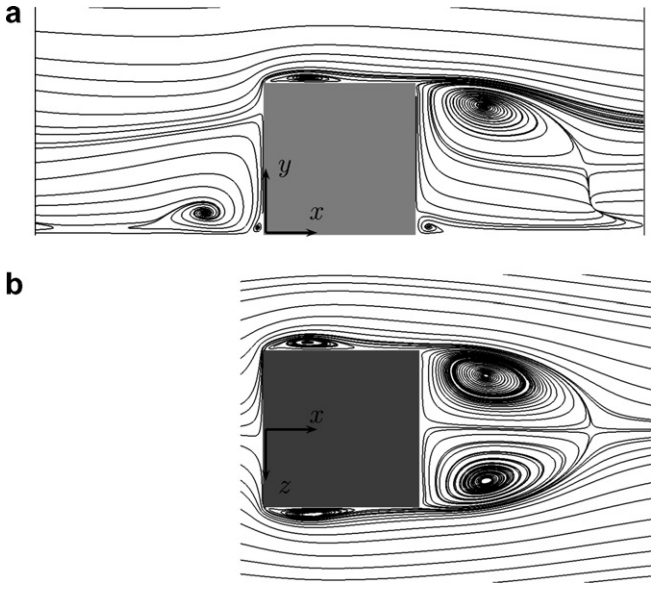

Fig. 6. Cube without VG. Time-averaged streamlines projected to: (a) the xy-plane at $z/H = 0$ and (b) the xz-plane at $y/H = 0.5$.

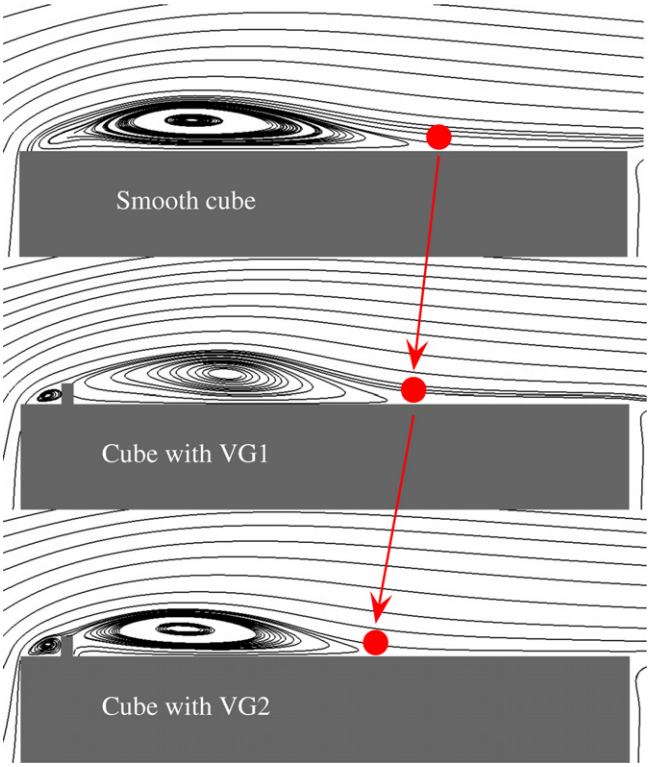

Fig. 7. Time-averaged streamlines projected to the xy-plane at $z/H = 0$ showing the separation region above the cubes with and without VGs.

regions more precisely. Fig. 7 shows the separation bubbles in the time-averaged flow above the top-side faces for a cube without VG, a cube with VG1 and a cube with VG2.

The points where the flow reattaches to the surface of the cube are marked in Fig. 7 to highlight the differences in the size of the separation bubbles. Obviously, the length of the separated flow is longest for the smooth cube and decreases considerably when VGs are attached to the surface of the cube. Although the shapes of the separation bubbles look similar in time-averaged flow, the temporal evolution of these bubbles is completely different. In the case of a smooth cube without VG, the flow separates from the faces only at the sharp edges of the cube. In contrast, the bubbles that appear in the time-averaged flow on the top and side faces of cubes with VGs are not only a result of the separation from the sharp edges of the large cube but also occur because of the shedding of small vortices from the vortex generators.

Fig. 8 is a snapshot showing instantaneous streamlines in the separation regions above the cubes. Different snapshots corresponding to other time steps, similar to that seen in Fig. 8 (not shown here), show that the temporal behaviors of the separation bubbles are different. In the case of a smooth cube, there is a periodic behavior of the separation regions. Their sizes change at a regular frequency that is equal to the shedding frequency from the previous cube. On the other hand, the separation regions behind the VGs are characterized by unsteady vortices. These vortices are shed from the recirculation regions behind the VGs to the boundary layer of the cube. The shedding frequency of these vortices is much higher than the dominant shedding frequency of the flow behind the large cubes. The flow structures over and around the cubes with VGs are much more complex and turbulent than those around the smooth cube.

Fig. 9 shows the flow structures around the different cubes by means of the isosurface of the positive second-invariant of the velocity gradient, $Q = -1/2\partial u_i/\partial x_j \partial u_j/\partial x_i$.

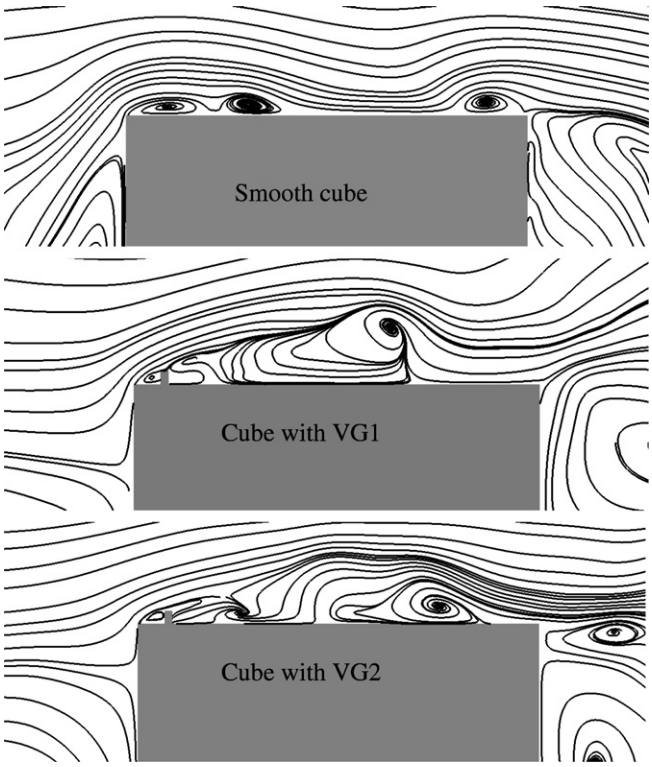

Fig. 8. Instantaneous streamlines projected to the *xy*-plane at $z/H = 0$ showing the flow structures above the cubes with and without the VGs.

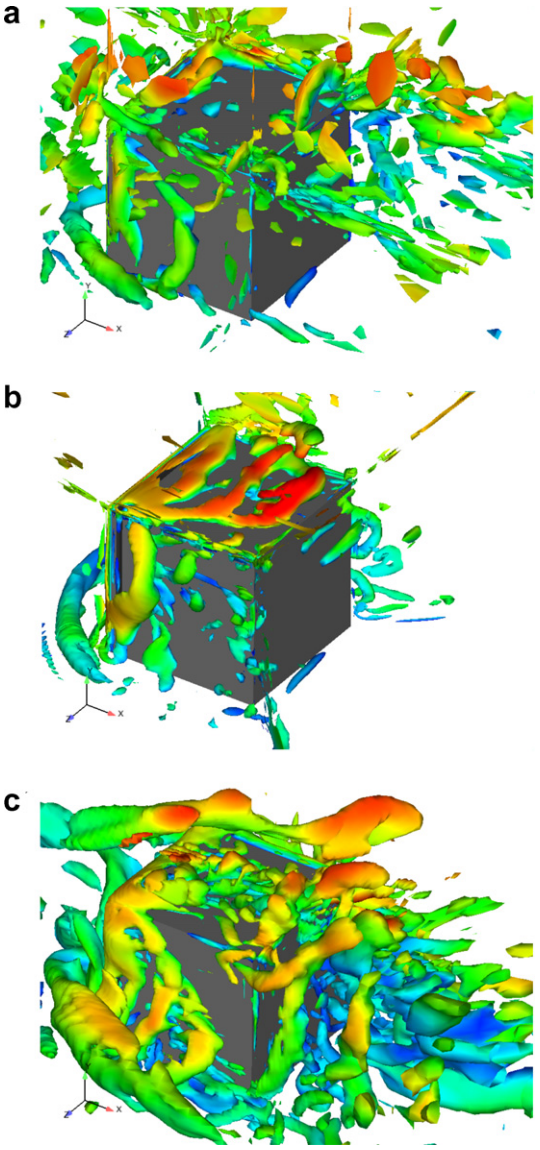

Fig. 9. Isosurface of the positive second-invariant of the velocity gradient, $Q = 10{,}000$ colored by velocity magnitude: (a) smooth cube, (b) cube with VG1 and (c) cube with VG2.

In the case of the smooth cube (Fig. 9a), most of the flow structures are detached from the surface of the cube and they are generated by the separation at the windward edge of the cube, the shedding of large vortices from the previous cube and the Kelvin–Helomholtz instability in the shear layer between the separated flow and the exterior fluid. In the case of the cube with VG1 (Fig. 9b), the separated flow behind the vortex generator is attached to the surface of the cube. These structures are elongated in the span-wise direction on the top-side face. They move towards the center of the cube downstream of the vortex generator. More flow structures can be seen close the surface of the cube in the case of VG2 (Fig. 9c) than are seen in Fig. 9a and b. These structures are elongated in the stream-wise direction. They are also larger in size than those in Fig. 9a and b. These large structures on the boundary layer help to carry the heat from the surface of the cube to the far cold stream and hence increase the heat transfer coefficient on the surface of the cube.

In order to see the difference in the flow characteristics behind the VGs, the stream-wise velocity, U_x, at $x/H = 0.5$, $y/H = 1.033$ and $z/H = 0$ is recorded during the simulation. The chosen point is at the center of the cube in the *xz*-plane, 0.5 mm above the large cube. This position is in the shear layer flow between the recirculation regions behind the VGs and their surrounding flow. Figs. 10a–12a show the time history of the stream-wise velocity at the reference point in the cases of the cube without VG, the cube with VG1 and the cube with VG2, respectively.

In addition to the time history of the steam-wise velocity components, Figs. 10b, 11b and 12b show the corresponding power spectra of the velocity component. It can be seen in Fig. 10b that the dominating flow frequency corresponds to a Strouhal number, *St*, of 0.109. This frequency is equal to the shedding frequency from the large cubes and is in agreement with the experimental data. The reliability of the lower dominating frequency in Fig. 10b is poor owing to the short time period monitored in the simulation. On the other hand, the dominating frequencies in the case of cubes with VGs are much higher than those of the cube without VGs. Fig. 11b shows the dominating frequencies corresponding to Strouhal numbers $0.12 < St < 0.7$. Moreover, the dominating frequencies for the cube with VG2 correspond to Strouhal numbers of $0.12 < St < 0.6$, as shown in Fig. 12b. Fig. 11b shows that the cube with VG1 has somewhat higher dominant frequencies than the cube with VG2, as shown in Fig. 12b. These frequencies are associated with the shear layer instabilities, indicating that the flow above the cube with VG1 is more turbulent than the flow over the cube without VGs and the cube with VG2.

Fig. 13 shows the time-averaged temperature profiles in the boundary layer around the cubes on the vertical *xy*-plane at $z/H = 0$. High temperature spots are found on the surface of the cube at the places where the flow separates or circulates. Despite the existence of a higher temperature spot behind the VG1, the time-averaged temperature distributions close to the cubes with VGs are globally lower than that around the cube without VG. In the recirculation region behind VG1, the heated air is trapped inside the circulating flow, which raises the surface temperature in this

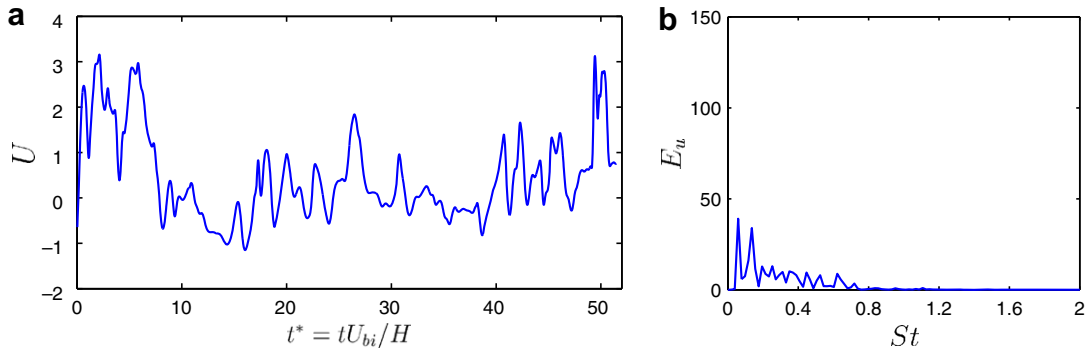

Fig. 10. Cube without VG: (a) time history of the stream-wise component of the velocity at $x/H = 0.5$, $y/H = 1.033$ and $z/H = 0$ and (b) the corresponding power spectra.

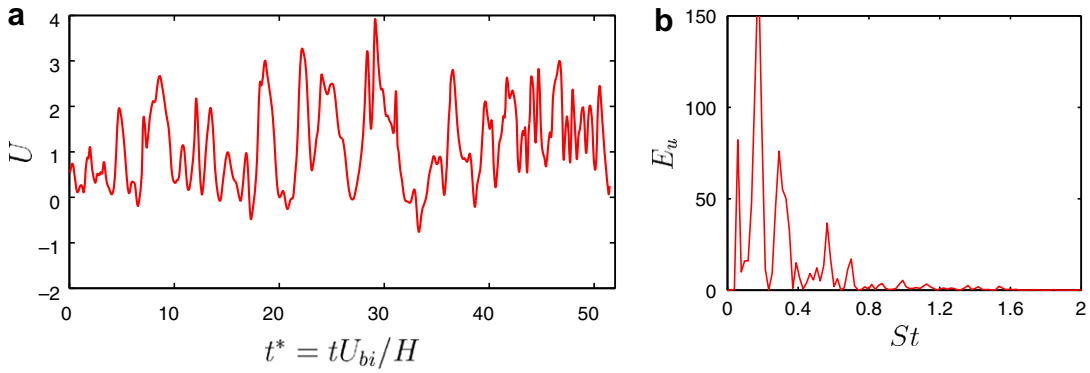

Fig. 11. Cube with VG1: (a) time history of the stream-wise component of the velocity at $x/H = 0.5$, $y/H = 1.033$ and $z/H = 0$ and (b) the corresponding power spectra.

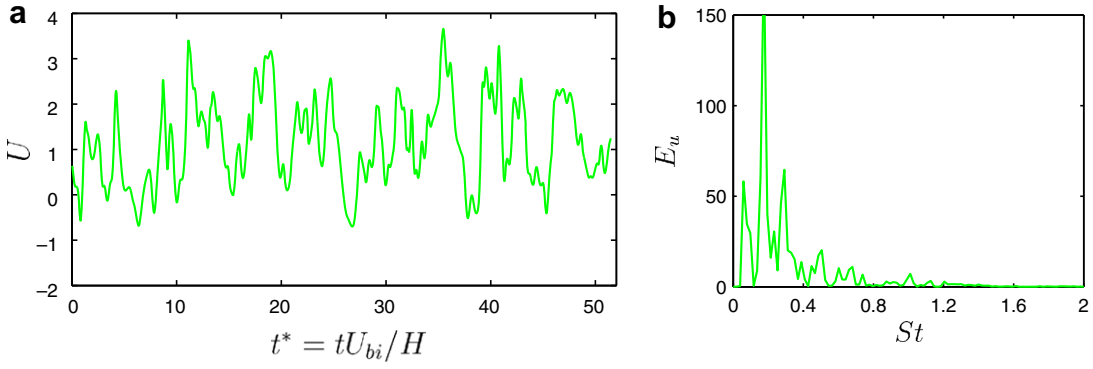

Fig. 12. Cube with VG2: (a) time history of the stream-wise component of the velocity at $x/H = 0.5$, $y/H = 1.033$ and $z/H = 0$ and (b) the corresponding power spectra.

region. The temperature around the cube with VG2 is lower than that of the cube without VGs and that of the cube with VG1, as shown in Fig. 13.

Shedding of vortices from the VGs not only changes the structure of the turbulent boundary layer but also the structures of the wake flow. This influences the temperature distribution in the wake flow. This can be seen in Fig. 13 as a reduction of the temperature on the stream-wise and lee-side faces of the cube with VGs.

The difference between the temperature of the surface of the cubes and the inlet bulk temperature is used to calculate the local heat transfer coefficient h as

$$h = \frac{q}{T_s - T_{bi}}. \tag{9}$$

Here q, T_s and T_{bi} are the heat flux, the surface temperature and the inlet bulk temperature, respectively. In this way, the heat transfer coefficient is a direct measure of the surface temperature and is suitable for judging the performance of the VGs.

To identify the relation between the flow structures and the temperature distribution and hence the heat transfer, the values of the local heat transfer coefficient at three different cross sections of the cube are shown in Fig. 14. As noted earlier, the temperature of the surface of the cubes is high at locations associated with flow separations. This is shown by low heat transfer coefficients on the lateral and top-side faces close to the leading edges and on the lee-side face next to the arch-like vortex. Fig. 14b shows a lower heat transfer coefficient behind the VG1, while Fig. 14 displays a more evenly distributed heat transfer coefficient over all sides of the cube.

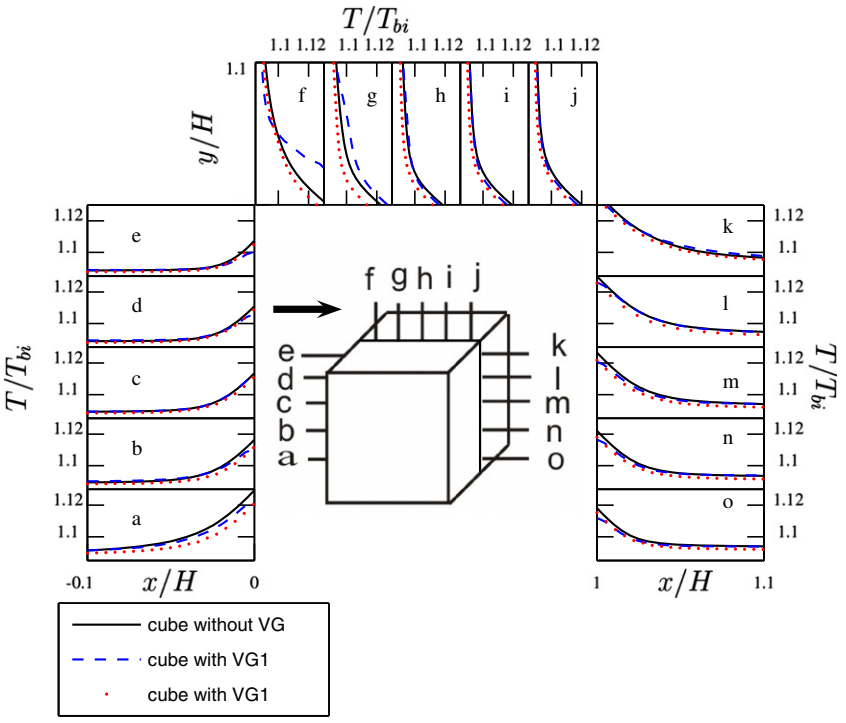

Fig. 13. Time-averaged temperature distribution at different positions on the *xy*-plane at $z/H = 0$ showing the thermal boundary layers obtained from the different cube configurations.

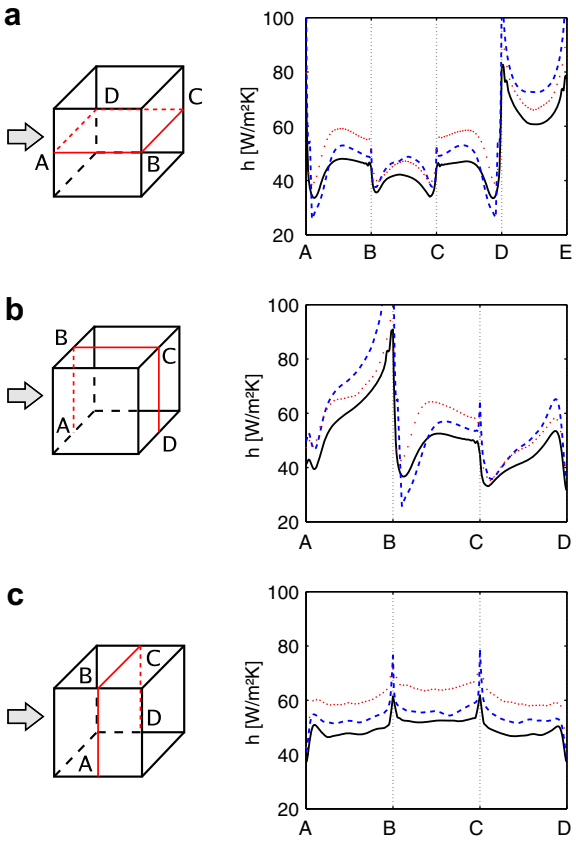

Fig. 14. Distribution of the time-averaged local heat transfer coefficient along: (a) path ABCDA on the horizontal *xz*-plane at $y/H = 0.5$, (b) path ABCD on the vertical *xy*-plane at $z/H = 0$ and (c) path ABCD on the vertical *yz*-plane at $x/H = 0.5$. Solid lines (LES over a smooth cube); dashed lines (LES over a cube with VG1); dotted lines (LES over a cube with VG2).

Table 2
Mean heat transfer coefficient on each face of the cube

Cube face	Cube without VG	Cube with VGI	Cube with VG2
Front	66	82.8	73.3
Top	50	53	59.8
Lee-side	38.8	44.2	43
Lateral sides	45	49	54.7
Cube average	48.9	55.6	57.1

Table 3
The percentage increase of the mean heat transfer coefficient

Cube face	Without VG to VGI	VG1 to VG2	Without VG to VG2
Front	25.7	−11	11.1
Top	6.4	12.9	20.1
Lee-side	13.9	−2.6	10.9
Lateral sides	8.9	11.5	21.4
Cube average	13.7	2.6	16.7

The space average of the time-averaged heat transfer coefficient over the different faces of the cubes is given in Table 2. Table 3 lists the percentage increase of the averaged heat transfer coefficient between the different cube configurations.

Although there are local high temperature spots behind the VG1 that are associated with a decrease in the local heat transfer coefficient, the global mean heat transfer coefficient is higher on all the faces than the mean heat transfer coefficient of the cube without VGs. Table 3 shows that the great enhancement of the mean heat transfer coefficient on the front and the back-side faces are found with the cube with VG1, where there is an increase of about 25.7% on the front face while an increase of about 13.9% is found on the back-side face. The largest percentage increase of the mean heat transfer coefficient in the case of the cube with VG2 is found to be about 21% on the lateral and the top-side faces. Globally, the

enhancement of the heat transfer coefficient is about 13.7% using VG1 and about 16.7% using VG2.

8. Conclusion

Large-eddy simulation was successfully used to investigate the influence on the local heat transfer by attaching vortex generators to the surface of wall-mounted heated cubes. Two different vortex generator shapes were investigated: a simple rib VG and a VG with the shape of a small cube. A mesh topology consisting of *C* and *O*-grids was used in the simulations, which considerably reduced the number of cells needed for good spatial resolution. LES results for flow and temperature distributions were obtained for surface-mounted cubes with and without a vortex generator. Two computations using different meshes around the cube with VG2 showed mesh-independent results. The LES results were found to be in good agreement with the experimental data for the cube without VG, for which the experimental data exists.

The relation between the flow structures around the cube and the temperature distribution is explained in the paper. The stream-wise faces of the cubes were found to have high heat transfer coefficients due to the down-wash flow that efficiently carries the heat from the face. Lower local heat transfer coefficients are reported at places where flow separation occurs, such as at the lee-side face of the cube close to the arch-shaped vortex.

Attaching vortex generators to the top and lateral faces of the cube resulted in a shorter distance of flow separation at these faces. This led to an increase in the local heat transfer coefficient.

It was found that the VGs altered the boundary layer on the surface of the cube. As a result, vortices were shed from the wake of the VGs at a higher frequency than the dominant vortex shedding in the flow. Globally, these vortices enhanced the mixing of heat in the boundary layer, which appeared as high mean heat transfer coefficients.

The present investigation showed that the percentage increase in the heat transfer coefficient was considerable with both kinds of vortex generators.

Local high temperature spots were found close to the circulation region behind the rib-shaped vortex generator (VG1), but the temperature distribution at the cube with the second vortex generator (VG2) was found to be more evenly distributed. Hence, the problem of local overheating behind VG1 disappeared when VG2 was used.

There was an increase in the mean heat transfer coefficient caused by the attachment of the VG1 and the attachment of VG2 to the surface of the cube of about 13.7% and 16.7%, respectively.

Acknowledgement

The research presented in this paper was supported by the Swedish Agency for Innovation System (VINNOVA), Scania, Bombardier Transportation and ANSYS Sweden. Computer time on HELIOS, the Linux cluster provided by C3SE at Chalmers University, is gratefully acknowledged. The authors are grateful to Professor Lars Davidson for valuable discussions.

References

Barhaghi, D.G., Davidson, L., Karlsson, R., 2006. Large-eddy simulation of natural convection boundary layer on a vertical cylinder. International Journal of Heat and Fluid Flow 27, 811–820.

Cheng, Y., Lien, F., Yee, E., Sinclair, R., 2003. A comparison of large-eddy simulations with a standard $k-\epsilon$ Reynolds-Averaged Navier–Stokes model for the prediction of a fully developed turbulent flow over a matrix of cubes. Journal of Wind Engineering and Industrial Aerodynamics 91, 1301–1328.

Hemida, H., Krajnović, S., Davidson, L., 2005. Large-eddy simulations of the flow around a simplified high speed train under the influence of a cross-wind. In: 17th AIAA Computational Fluid Dynamics Conference, Toronto, Ontario, Canada, June 6–9.

Krajnović, S., Davidson, L., 2000. Flow around a three-dimensional bluff body. In: Ninth International Symposium on Flow Visualization.

Krajnović, S., Davidson, L., 2002. Large-eddy simulation of the flow around a bluff body. AIAA Journal 40 (5), 927–936.

Krajnović, S., Davidson, L., tul=0?>Krajnović and Davidson, 2005. Flow around a simplified car, part 1: Large-eddy simulation. ASME: Journal of Fluids Engineering 127, 907–918.

Martinuzzi, R., Tropea, C., 1993. The flow around surface-mounted prismatic obstacles placed in a fully developed channel flow. ASME: Journal of Fluid Engineering 115, 85–91.

Meinders, E.R., Hanjalić, K., tul=0?>Meinders and Hanjalić, 1999. Vortex structure and heat transfer from in-line and staggered configurations of two wall-mounted cubes. International Journal of Heat and Mass Transfer 20, 255–267.

Meinders, E.R., Hanjalić, K., tul=0?>Meinders and Hanjalić, 2002. Experimental study of the convective heat transfer from in-line and staggered configurations of two wall-mounted cubes. International Journal of Heat and Mass Transfer 45, 465–482.

Nakamura, H., Igarashi, T., Tsutsui, T., 2003. Local heat transfer around a wall-mounted cube at 45° to flow in a turbulent boundary layer. International Journal of Heat and Fluid Flow 24, 807–815.

Ničeno, B., Dronkers, A.D.T., Hanjalić, K., 2002. Turbulent heat transfer from a multi-layered wall-mounted cube matrix: a large eddy simulation. International Journal of Fluid Flow 23, 173–185.

Verstappen, R.W.C.P, Van der Velde, R.M., Veldman, A.E.P., 2000. DNS of turbulent flow and heat transfer in a channel with surface mounted cubes. In: ECCOMAS 2000, Barcelona, vol. 46, September 11–14, pp. 983–1005.

Wallin, F., Eriksson, L., 2006. A tuning-free body-force vortex generator model. In: 44th AIAA Aerospace Sciences Meeting and Exhibit, Reno, Nevada, January 9–12.

Yakhot, A., Liu, H., Nikitin, N., 2006. Turbulent flow around a wall-mounted cube: a direct numerical simulation. International Journal of Heat and Fluid Flow 27, 994–1009.

Zhong, B., Tucker, P.G., 2004. $k-l$ based hybrid LES/RANS approach and its application to heat transfer simulation. International Journal for Numerical Methods in Fluids 46, 983–1005.